Measurement Science
and Technology

ACCEPTED MANUSCRIPT • OPEN ACCESS

Temperature and pressure reconstruction in turbulent Rayleigh-Bénard convection by Lagrangian velocities using PINN

To cite this article before publication: Robin Barta *et al* 2025 *Meas. Sci. Technol.* in press https://doi.org/10.1088/1361-6501/adee38

Manuscript version: Accepted Manuscript

Accepted Manuscript is “the version of the article accepted for publication including all changes made as a result of the peer review process, and which may also include the addition to the article by IOP Publishing of a header, an article ID, a cover sheet and/or an ‘Accepted Manuscript’ watermark, but excluding any other editing, typesetting or other changes made by IOP Publishing and/or its licensors”

This Accepted Manuscript is **© 2025 The Author(s). Published by IOP Publishing Ltd**.

As the Version of Record of this article is going to be / has been published on a gold open access basis under a CC BY 4.0 licence, this Accepted Manuscript is available for reuse under a CC BY 4.0 licence immediately.

Everyone is permitted to use all or part of the original content in this article, provided that they adhere to all the terms of the licence https://creativecommons.org/licences/by/4.0

Although reasonable endeavours have been taken to obtain all necessary permissions from third parties to include their copyrighted content within this article, their full citation and copyright line may not be present in this Accepted Manuscript version. Before using any content from this article, please refer to the Version of Record on IOPscience once published for full citation and copyright details, as permissions may be required. All third party content is fully copyright protected and is not published on a gold open access basis under a CC BY licence, unless that is specifically stated in the figure caption in the Version of Record.

View the article online for updates and enhancements.

This content was downloaded from IP address 129.247.247.240 on 14/07/2025 at 10:29

Temperature and pressure reconstruction in turbulent Rayleigh-Bénard convection by Lagrangian velocities using PINN

R. Barta[1,2], **M.-C. Volk**[1,2], **C. Bauer**[1], **C. Wagner**[1,2] **and M. Mommert**[1]

[1] Institute of Aerodynamics and Flow Technology, German Aerospace Center (DLR), Bunsenstraße 10, Göttingen, 37073, Germany

[2] Technische Universität Ilmenau, Institute of Thermodynamics and Fluid Mechanics, Ilmenau, Germany

E-mail: `robin.barta@dlr.de`

Keywords: physics informed neural networks, data assimilation, particle tracking velocimetry, Rayleigh-Bénard convection, open-source

Abstract. Velocity, pressure, and temperature are the key variables for understanding thermal convection, and measuring them all is a complex task. In this paper, we demonstrate a method to reconstruct temperature and pressure fields based on given Lagrangian velocity data. A physics-informed neural network (PINN) based on a multilayer perceptron architecture and a periodic sine activation function is used to reconstruct both the temperature and the pressure for two cases of turbulent Rayleigh-Bénard convection ($\mathrm{Pr} = 6.9$, $\mathrm{Ra} = 10^9$). The first dataset is generated with DNS and it includes Lagrangian velocity data of 150000 tracer particles. The second contains a PTV experiment with the same system parameters in a water-filled cubic cell, and we observed about 50000 active particle tracks per time step with the open-source framework proPTV. A realistic temperature and pressure field could be reconstructed in both cases, which underlines the importance of PINNs also in the context of experimental data. In the case of the DNS, the reconstructed temperature and pressure fields show a 90% correlation over all particles when directly validated against the ground truth. Thus, the proposed method, in combination with particle tracking velocimetry, is able to provide velocity, temperature, and pressure fields in convective flows even in the hard turbulence regime. The PINN used in this paper is compatible with proPTV and is part of an open source project. It is available at `https://github.com/DLR-AS-BOA/RBC-PINN`.

1. Introduction

The velocity fields of flows can be measured precisely on temporal and spatial scales, for example, by particle tracking velocimetry (PTV). PTV (Maas et al., 1993; Malik et al., 1993; Schröder and Schanz, 2023) is a well-known optical measurement technique in experimental fluid mechanics to obtain Lagrangian velocity vector fields within observation domains by tracking the movement of tracer particles within a moving fluid over set time intervals. Many interesting flows in scientific or industrial contexts are thermally driven, such as Rayleigh-Bénard convection (RBC) or the mixed convective flow in the ventilation of closed passenger cabins (Schmeling et al., 2023). In both cases, it is much more difficult to measure the temperature field with the same resolution as the velocity fields, which can be achieved, for example, by using thermoliquid crystals as tracer particles for PTV (Käufer and Cierpka, 2023). This method is intriguing, but difficult to implement in general settings. Therefore, a more general approach to determine unknown flow properties such as temperature and pressure fields is to reconstruct them by enforcing the underlying governing equations, using known velocity data, typically facilitating physics-informed neural network (PINN) (Raissi et al., 2019). The PINN approach is rather new, but this topic has increased research activity and interests in recent years (Cai et al., 2021a). Notable examples, relevant for the present application to thermal convective flows, are the reconstruction of velocities from temperatures for synthetic 2D flows (Clark Di Leoni et al., 2023), the investigation of PINNs framework for full PDE modeling in turbulent convection flows (Lucor et al., 2022) or for background-orient Schlieren measurements (Cai et al., 2021b). The opposite reconstruction direction, temperature from velocities, is shown by Mommert et al. (2024) for a synthetic (DNS) case of cubic Rayleigh-Bénard convection and by Toscano et al. (2024) for a PTV measurement extended by temperatures from particle image thermometry. Volk et al. (2025) further showed for a synthetic case that this methodology can also be applied to the planar datasets of stereoscopic particle image velocimetry. In this paper, we build on previous validation studies of PINNs that reconstruct moderate turbulent Rayleigh-Bénard convection at medium Rayleigh numbers (Mommert et al., 2024; Toscano et al., 2025; Volk et al., 2025) by presenting an open-source PINN version, based on a multilayer perceptron architecture and a periodic sine activation function to assimilate both temperature and pressure from Lagrangian velocity data even in cases of fully turbulent Rayleigh-Bénard convection at high Rayleigh numbers. Although our PINN methodology has been shown to be effective at lower Rayleigh numbers, this elevated regime is a previously unexplored parameter space in which complex, multiscale turbulent dynamics pose significant computational challenges. We examine these difficulties and propose solutions to improve the reconstruction accuracy in this flow regime. The method is tested on two datasets in this paper: one generated with direct numerical simulations (DNS) and the other covering a PTV experiment (Barta and Wagner, 2025) of turbulent RBC in a cubic cell filled with water. Both datasets have Prandtl and Rayleigh numbers of $\mathrm{Pr} = 6.9$ and $\mathrm{Ra} = 10^9$, respectively.

RBC (Rayleigh, 1916) is a canonical system for studying thermal convection, in which a fluid is confined in a container and heated from below and cooled from above, ideally with adiabatic sidewalls. A unified theory that describes the scaling laws of the response parameter (Reynolds and Nusselt number) based on the system parameters in RBC was established by Grossmann and Lohse (2000). The set of flow-governing equations is given by the incompressible Navier-Stokes equation in the Oberbeck-Boussinesq approximation and the energy equation for the temperature, both in normalized units.

$$\frac{\partial \vec{u}}{\partial t} + (\vec{u} \cdot \nabla)\,\vec{u} = -\nabla p + \sqrt{\frac{\mathrm{Pr}}{\mathrm{Ra}}}\,\nabla^2 \vec{u} + T\vec{e}_Z, \tag{1}$$

$$\frac{\partial T}{\partial t} + \vec{u} \cdot \nabla T = \sqrt{\frac{1}{\mathrm{Pr}\,\mathrm{Ra}}}\,\nabla^2 T, \tag{2}$$

$$\nabla \cdot \vec{u} = 0. \tag{3}$$

Here, $\vec{e}_Z$ denotes the unit vector in the vertical direction. Each velocity in equations (1)-(3) has been non-dimensionalized with the free-fall velocity $u_{ref} = \sqrt{\lambda g \Delta T L}$, the three spatial coordinates with the cell height L, the time coordinate with the free-fall time $t_{ref} = L/u_{ref}$ and the pressure with the reference pressure $p_{ref} = \rho u_{ref}^2$, where ρ is the fluid density. The pressure is determined up to a constant value p_0 because only its gradient is present in equation (1), and in the following we set $p_0 = 0$. The temperature is always centered around the mean cell temperature and it is non-dimensionalized by the temperature difference $\Delta T = T_w - T_c$ between the heating (T_w) and cooling (T_c) plates, so that the non-dimensionalized temperature ranges between -0.5 and 0.5.
The two independent system parameters, Ra and Pr, are defined in the following way.

$$\mathrm{Ra} = \frac{g\,\lambda\,\Delta T\,L^3}{\nu\,\alpha}, \quad \mathrm{Pr} = \frac{\nu}{\alpha}. \tag{4}$$

In equation (4) g is the absolute value of the gravitational acceleration on Earth, λ is the coefficient of thermal expansion, ν is the kinematic viscosity and κ is the thermal diffusivity.
The paper is organized as follows. Section 2 introduces the DNS and experimental Rayleigh-Bénard convection datasets on which the PINN is applied. Section 3 explains the general PINN methodology, including the network architecture and the training routine. In section 4 the PINN is validated on DNS data and in section 5 the temperature and pressure reconstruction with the PINN is tested on experimental data. Finally, in section 6 a conclusion is drawn.

2. Rayleigh-Bénard convection datasets

In the following subsections, two datasets of turbulent Rayleigh-Bénard convection in a cubic cell (Ra = 10^9 and Pr = 6.9) on which the PINN is tested are presented, both containing particle tracks and providing velocities in the Lagrange frame. In the first dataset, the particle tracks are generated in a direct numerical simulation (DNS). The ground truth velocities, temperatures, and pressures are known exactly on the particle positions. The DNS dataset is used to validate the reconstructed temperature and pressure fields with the PINN. The second set contains particle tracks measured with proPTV (Barta et al., 2023) in a cubic cell filled with water (Barta and Wagner, 2025).

We choose a reconstruction interval for both data sets with a temporal length of at least $2\,t_{\mathrm{ref}}$, which was shown to be sufficient in (Volk et al., 2025).

2.1. DNS

The DNS is performed in a cubic RBC cell with isothermal heating and cooling plates and adiabatic side walls with $\mathrm{Ra} = 10^9$ and $\mathrm{Pr} = 6.9$. The DNS solves the dimensionless transport equations for mass, momentum, and temperature for an incompressible fluid using the Oberbeck-Boussinesq approximation, see equations (1)-(3). At all walls, no-slip and impermeability boundary conditions are applied. Furthermore, the dimensionless set of equation (1)-(3) are discretized spatially with fourth-order central differences and in time using a second-order accurate Euler-leapfrog scheme (Wagner et al., 1994). The DNS is performed similarly as discussed in more detail in (Barta et al., 2023) but here for smaller Ra. For the present case of $\mathrm{Pr} > 1$, the global mean Batchelor length scale (Scheel et al., 2013):

$$\eta_B = \eta\,\mathrm{Pr}^{-1/2} = \frac{1}{\mathrm{Ra}^{1/4}\,(\mathrm{Nu}-1)^{1/4}}, \tag{5}$$

is smaller than the Kolmogorov length scale η, and thus more restrictive with respect to the grid resolution. The Batchelor length η_B represents the smallest length scale at which temperature fluctuations exist before being dissipated by thermal diffusion. Therefore, the minimum grid spacing in the bulk flow region was estimated to resolve the Batchelor scale according to Grötzbach (1983) and Scheel et al. (2013). Furthermore, the minimum grid spacing in the thermal and viscous boundary layers has been estimated according to Shishkina et al. (2010). For the grid estimation, the Nusselt number can be estimated a priori from the Grossmann-Lohse theory (Grossmann and Lohse, 2000, 2001, 2002, 2004), resulting in $\mathrm{Nu} = 61$, which is similar to the Nusselt number calculated a posteriori:

$$\mathrm{Nu} = \left\langle \sqrt{\mathrm{Ra}\,\mathrm{Pr}}\,T\,\vec{u}\cdot\vec{e}_Z - \frac{\partial T}{\partial Z} \right\rangle_{XYZt} \tag{6}$$

where $\langle\cdot\rangle_{XYZt}$ denotes averaging in time, as well as in the X, Y and Z directions, resulting in $\mathrm{Nu} = 63.4$. Table 1 summarizes the simulation parameters, including grid spacing and the number of grid points in the thermal and kinetic boundary layer.

Ra	Pr	$N_X \times N_Y \times N_Z$	Δt	Δt_{out}	$\Delta Z_{\mathrm{min}}/L$	$\Delta Z_{\mathrm{max}}/L$	N_{l_T}	N_{l_U}	Nu
10^9	6.9	$768 \times 768 \times 768$	10^{-4}	0.02	$4.5 \cdot 10^{-4}$	$2 \cdot 10^{-3}$	18	25	63.4

Table 1. Ra is the Rayleigh, Pr the Prandtl number. N_X, N_Y and N_Z are the number of grid points in X, Y, and Z direction, respectively. Δt is the temporal resolution and Δt_{out} is the temporal output resolution of the particle tracks. ΔZ_{min} is the grid spacing at the plates, ΔZ_{max} is the grid spacing at the center of the box. N_{l_T} is the number of grid points in the thermal, N_{l_U} in the kinetic boundary layer. The Nusselt number is computed a posteriori.

After an initial transient, when the average Nusselt number computed reached a statistically stationary state, instantaneous flow field realizations in the form of velocity, pressure, and temperature fields are interpolated on 150000 massless tracer particle positions (chosen randomly inside the cubic domain), which are tracked in time. Figure 1 shows all tracks colored by their vertical velocity. Every $\Delta t_{out} = 0.02$ dimensionless time units, corresponding to a recording frequency of about 8 Hz in the experiment, a particle file is saved for the following analysis, where 125 particle files are used.

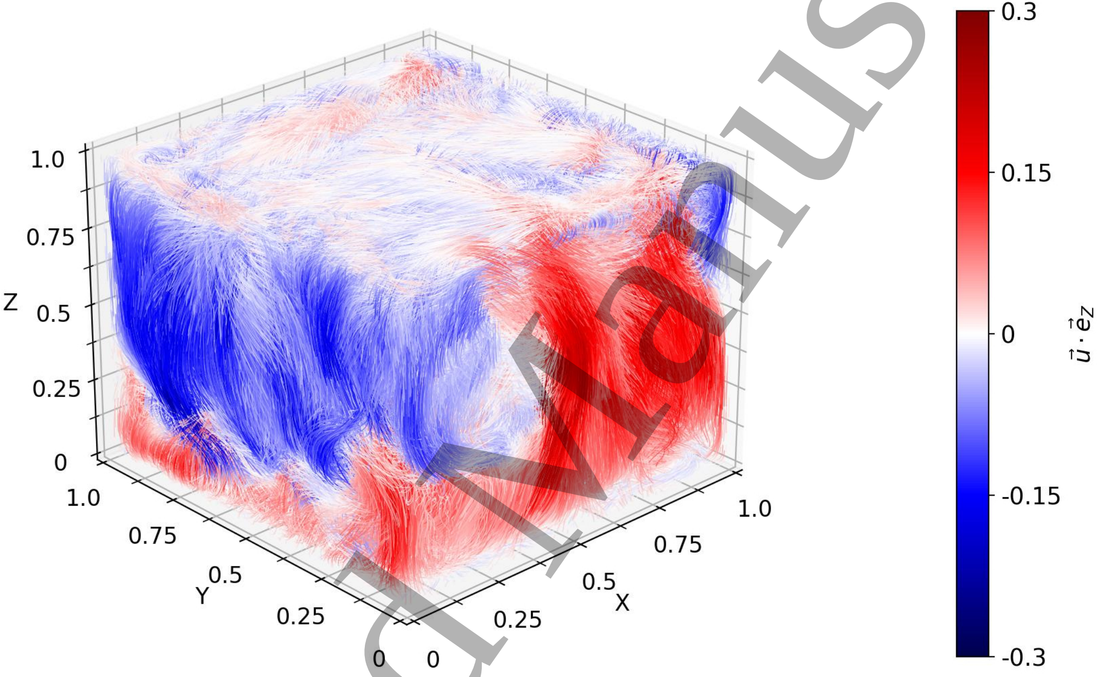

Figure 1. All tracks generated with DNS colored by their vertical velocity.

2.2. PTV experiment

The PTV experiment is the same water-filled cubic Rayleigh-Bénard convection cell as discussed in Barta and Wagner (2025), except here we use a temperature gradient between the heating and cooling plate of $\Delta T \approx 4\,\mathrm{K}$, and a recoding frequency of $f = 10\,\mathrm{Hz}$. The cell height of the cubic cell is $L = 300$ mm, and for the flow we estimate the free fall velocity $u_{ref} \approx 50\,\mathrm{mm\,s^{-1}}$ and the free fall time $t_{ref} \approx 6$ s. For the temperature difference considered, the Oberbeck-Boussinesq approximation (1)-(3) is valid, as shown in Gray and Giorgini (1976); Weiss et al. (2024). We estimate Ra $\approx 10^9$ and Pr ≈ 6.9 which is similar to the DNS, see Section 2.1. Figure 2 shows a technical drawing of the experimental setup and the reference coordinate system. The PTV sequence studied in this work consists of 150 time steps, and image acquisition began after the flow reached equilibrium, approximately 10 hours after seeding tracer particles. In total, 4 PCO Edge 5.5 cameras are observing the flow and each of them has a resolution of 2560×2160 pixels. Polyamide particles manufactured by LaVision with a density of 1.03 g cm^{-3}) are used as seeding material. PTV processing is performed using the open source framework proPTV (Barta et al., 2023) and the backtracking routine is used. The image processing detected about 110000 particles per camera. Camera calibration is performed using the built-in Soloff calibration model (Herzog et al., 2021; Soloff et al., 1997) with a calibration target of 19×19 imprinted markers shifted through the cell at 5 depth positions relative to the cameras, see Barta and Wagner (2025). Furthermore, a volumetric correction is applied using particle images such as in Wieneke (2008) and a subpixel calibration error of less than 0.1 pixels per camera is achieved.

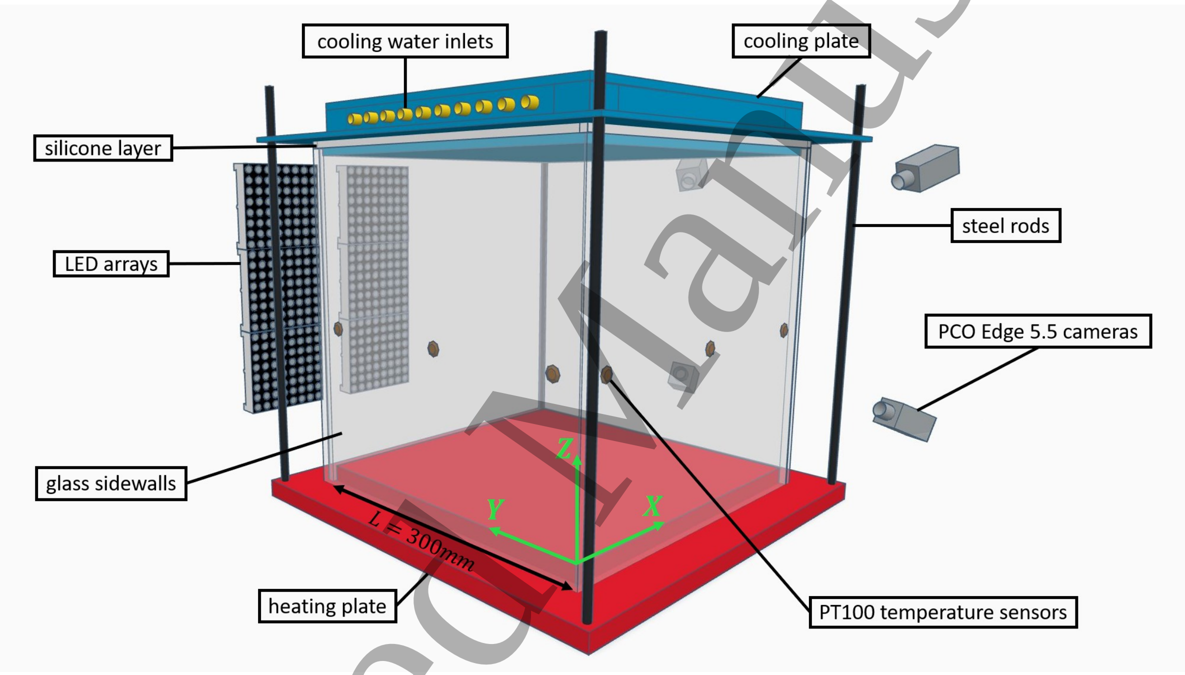

Figure 2. Technical drawing of the Rayleigh-Bénard experiment. A cubic cell filled with water and heated from below and cooled from above, four cameras observing the flow and two LED arrays illuminating the flow. The green arrows indicate the reference coordinate system.

Figure 3 provides an overview of the number of triangulated particles, initialized tracks, active tracks, and broken tracks during PTV processing of the 150 time steps. Almost all particles in the camera images are used to triangulate about 100000 particles per time step, from which about 50000 active tracks per time step are reached after processing the 25th time step. The new initialized tracks and broken tracks per time step are each about 3000 tracks after the 25th time step, so that about 5% of the tracks break each time step. All tracks obtained by processing the 150 time steps with proPTV are visualized in figure 4, and are colored by their normalized vertical velocity. In units, the maximum observed velocity is about ±10 m s^{-1}. During processing, a track is only accepted if it persists for at least 10 time steps. In total about 300000 particle tracks are reconstructed. The track density is high in the bulk flow (about 0.046 ppp), but the track density decreases drastically near the sidewalls because it is observed that the seeding material mostly sticks to the sidewalls when it enters the boundary layer and no reasonable resolution of the flow near the boundaries is achieved.

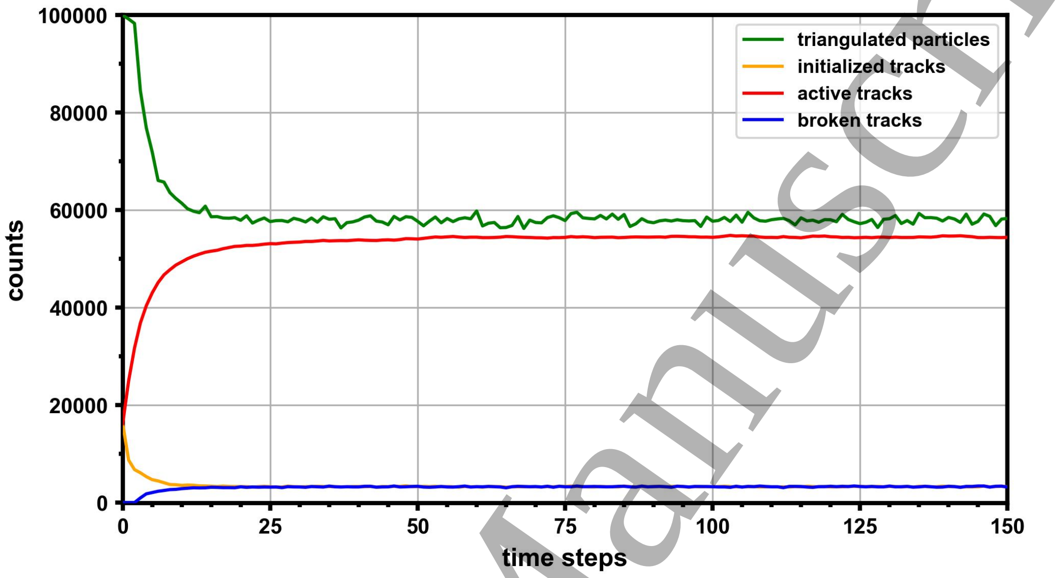

Figure 3. The number of triangulated particles, initialized tracks, active tracks and broken tracks per time step while processing the PTV dataset with proPTV.

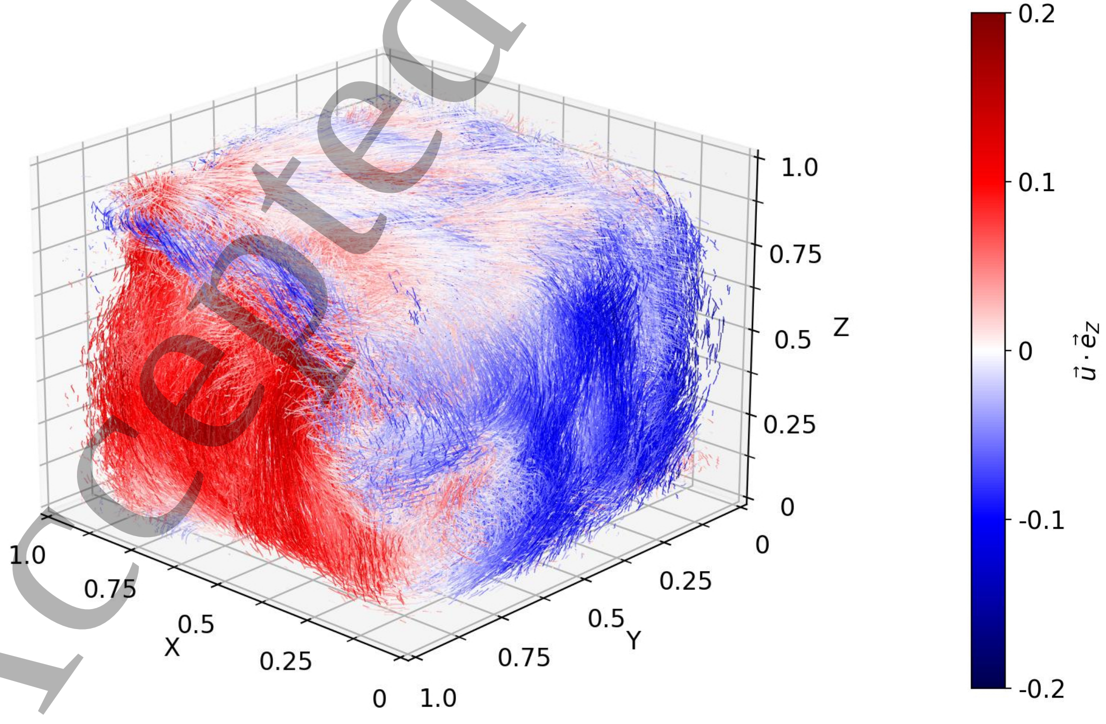

Figure 4. All PTV tracks colored by their normalized vertical velocity.

In figure 5 the track length histogram is shown and an average track length of 26 is calculated.

In the experiment, the velocity field has full temporal resolution. This is verified because the smallest velocity time scale is larger than the recording time: $\eta/U = 0.16\,\mathrm{s} > 1/f$, with the mean expected Kolmogorov length in the bulk of $\eta = 1.6\,\mathrm{mm}$ estimated using equation (5) and the maximum measured velocity magnitude $U \approx 10$ m s^{-1}. A full spatial resolution of the velocity field is not reached as it would require at least one particle in each volume cell spanned by the Kolmogorov length, or $(L/\eta - 1)^3 \approx 186^3 = 6435856$ particles. However, the most important structures are the large scale circulation and the corner circulations, which are both integral flow structures and those are well-resolved in our measurement.

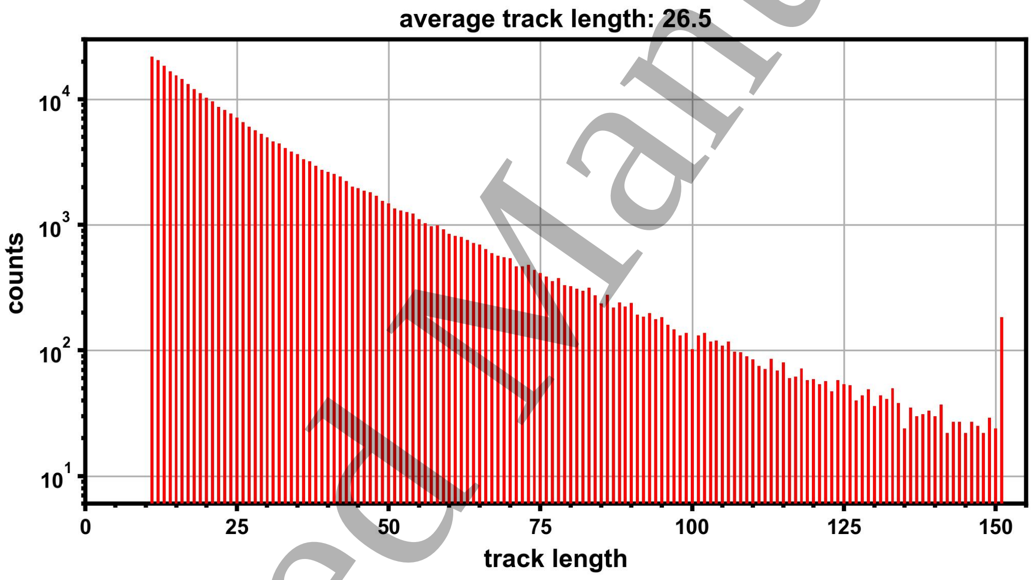

Figure 5. Track length histogram. The average track length is about 26.

3. PINN Methodology

3.1. Architecture

A multi-layer perceptron (MLP) is used to reconstruct unknown flow fields, such as temperature and pressure fields from known velocity fields. The MLP, shown in figure 6, consists of an input layer with 4 neurons corresponding to the time t and position coordinates: X, Y, Z, N_L fully-connected hidden layers each with a constant width of N_N neurons, and an output layer with 5 neurons corresponding to the approximated velocity field components u, v, w, temperature field T and pressure field p. In this paper, we use $N_L = 10$ and $N_N = 256$. The activation function used is the periodic sine function: $\sigma(\cdot) = \sin(\cdot)$. Sine activation functions are resistant to the vanishing gradient problem (Sitzmann et al., 2020), as their derivative is only close to zero in small periodic regions. The sine activation function helps the MLP to quickly develop an approximation function as a superposition of a large number of wavenumbers, which helps identify multiple structures in turbulent flows. The output layer is linearly activated and does not use an activation function. It should be noted that the proposed PINN architecture can be easily modified to reconstruct only the pressure if necessary.

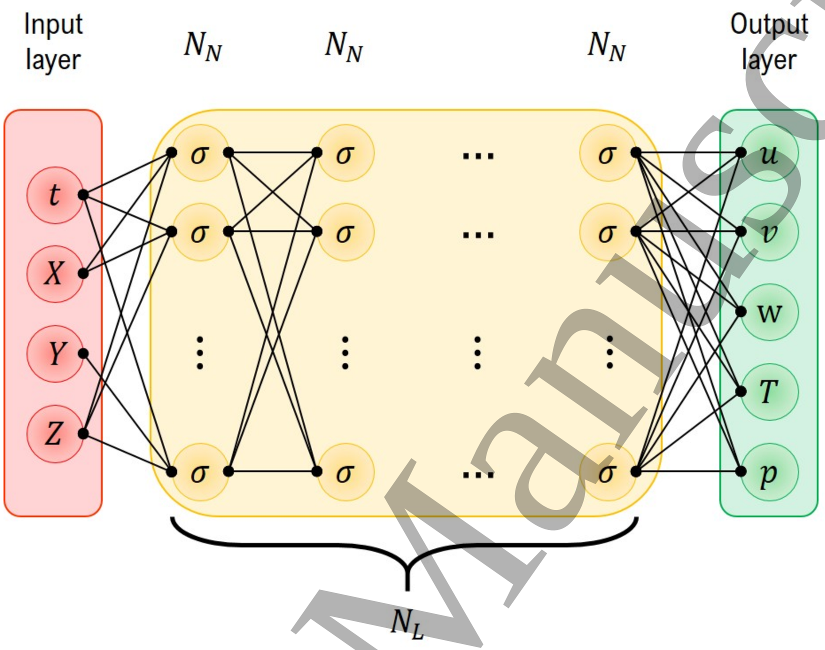

Figure 6. Architecture of the MLP used as physics-informed neural network to assimilate temperature and pressure with N_N neurons per hidden layer, N_L hidden layers, and a sinus activation function: $\sigma(\cdot) = \sin(\cdot)$.

The network is an extension of the method introduced by Mommert et al. (2024), and it was demonstrated (Mommert et al., 2024; Volk et al., 2025) that the PINN can learn the temperature and pressure fields from the provided velocity fields in the cases of RBC in the soft turbulence regime with low to medium Rayleigh numbers and a moderately complex loss landscape, the multidimensional optimization manifold representing how well the PINN satisfies physics constraints and data requirements, spanned by the loss function (10). That the simultaneous temperature and pressure reconstruction performs well in such cases is still remarkable because the model solves an ambiguity in the fundamental equations, since both temperature and pressure are unknown and both variables are in the same equation (1). However, the reconstruction of both temperature and pressure becomes problematic in RBC at high Rayleigh numbers, particularly in the hard turbulence regime $\mathrm{Ra} > 4 \cdot 10^7$ (Castaing et al., 1989), since then the loss landscape becomes more complex due to many small-scale flow structures that need to be reconstructed. Additionally, the high temperature gradients near the heating and cooling walls such as the near zero temperature in the well-mixed bulk are numerically difficult to resolve, and the reconstruction of both pressure and temperature are extremely challenging for a PINN. We address this problem by introducing a mean temperature profile to the PINN, and only the correct temperature fluctuations in addition to the pressure need to be learned. Thus, the temperature output of the PINN is modified by:

$$T = T_{\mathrm{mean}}(Z,a) + \left(Z^2 - Z\right)\, T' \tag{7}$$

$$\text{with} \quad T_{\mathrm{mean}}(Z,a) = \frac{1}{2 - 2\,\mathrm{e}^{-0.5\,a}} \begin{cases} \mathrm{e}^{-a\,Z} - \mathrm{e}^{-0.5\,a} & \text{, if } Z < 0.5 \\ \mathrm{e}^{-0.5\,a} - \mathrm{e}^{a\,(Z-1)} & \text{, if } Z \geq 0.5 \end{cases} \tag{8}$$

representing a mean temperature profile along the vertical Z axis, T' represents the temperature fluctuation field, and a is a user-defined parameter. A similar approach was used by Toscano et al. (2024), but they proposed to prescribe a linear mean temperature profile which turned out to be not helpful in the present case at $\mathrm{Ra} = 10^9$. Equation (7) is chosen empirically and ensures that the temperature boundary conditions are satisfied exactly. The physical meaning of a is derived by evaluating equation (6) on the heating or cooling plate where the velocity is zero, and using the derivative of equation (7) with respect to Z. Thus, we can relate the parameter a with the Nusselt number:

$$\mathrm{Nu} = \frac{a}{2 - 2\,\mathrm{e}^{-0.5\,a}} \simeq \frac{a}{2}\,, \quad \text{if} \quad a \gg 1\,, \tag{9}$$

and set $a = 2\,\mathrm{Nu} = 126$ throughout the paper, because we know that the average Nusselt number is $\mathrm{Nu} = 63$ obtained from DNS in our case, see section 2.1. Figure 7 illustrates how the mean temperature profile evolves as the Nusselt number in terms of the parameter a increases. Note that the parameter value $a = 1$ results in a linear temperature profile, similar to the one used by Toscano et al. (2024).

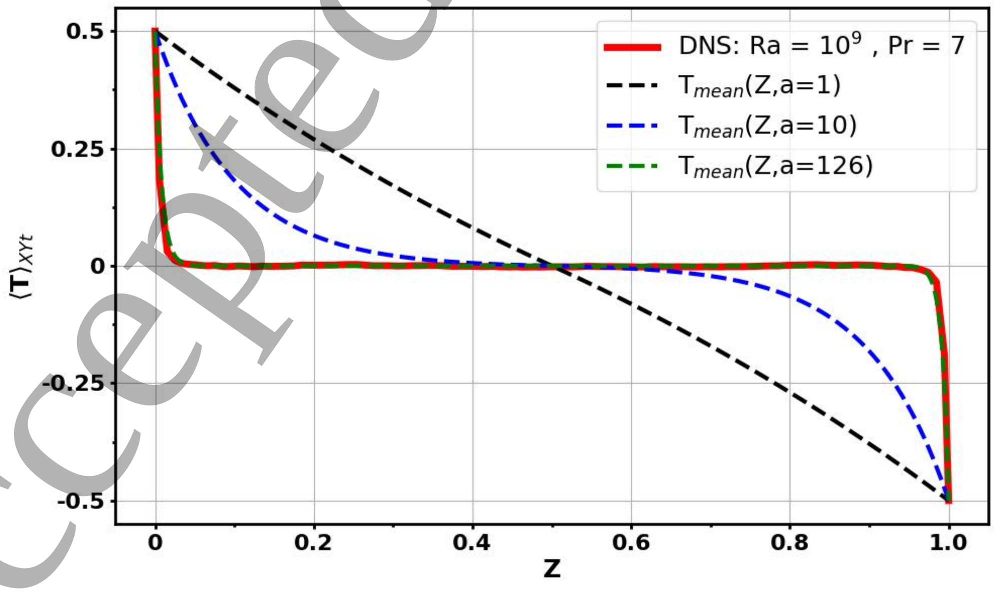

Figure 7. The mean temperature profile as a function of the vertical cell direction Z averaged with respect to time and the horizontal plane defined by the coordinates X and Y predicted in the DNS for $\mathrm{Ra} = 10^9$ and $\mathrm{Pr} = 6.9$. The empirical function $T_{\mathrm{mean}}(Z,a)$ is shown as dashed lines with increasing values of the parameter a.

3.2. Training and optimization

The purpose of the PINN is to reconstruct the temperature and pressure fields based on velocity fields obtained from experiments or flow simulations using the flow-governing equations of RBC in dimensionless units (1)-(3). The training of the PINN over N_{epoch} epochs is implemented in a Python framework using Tensorflow v.2.16 and Keras v.3.4 (Abadi et al., 2016; Chollet et al., 2015) with the MLP architecture described in section 3.1. Specifically, the Adam optimizer (Kingma and Ba, 2014) is used in the default configuration, except for a learning rate schedule that starts with a learning rate, usually $\text{lr}_{\text{max}} = 10^{-3}$, and reduces it by a factor of 0.8 until it reaches a certain value, usually $\text{lr}_{\text{min}} = 10^{-4}$. The learning rate reduction is applied after N_{lr} epochs of training have passed. A constant batch size of $N_B = 4096$ data points is used, which is a small fraction of the dataset studied. A smaller batch size means more optimization runs per epoch, which accelerates convergence (Sankaran et al., 2022) at the cost of computing time. The optimization of the internal PINN parameters is done by optimizing the following total loss function.

$$\mathcal{L}_{\text{tot}} = \lambda_{\text{data}}\,\mathcal{L}_{\text{data}} + \lambda_{\text{NS}}\,\mathcal{L}_{\text{NS}} + \lambda_{\text{EE}}\,\mathcal{L}_{\text{EE}} + \lambda_{\text{div}}\,\mathcal{L}_{\text{div}} + \lambda_{\text{C}}\,\mathcal{L}_{\text{C}} + \lambda_{\text{BC}}\,\mathcal{L}_{\text{BC}} \tag{10}$$

$$\mathcal{L}_{\text{data}} = \frac{1}{3\,N_B}\sum_{i=1}^{N_B} \left\|(\vec{u}_i - \vec{u}_i^*)^2\right\| \tag{11}$$

$$\mathcal{L}_{\text{NS}} = \frac{1}{N_B}\sum_{i=1}^{N_B^{\text{col}}} \left\|\left(\frac{\partial\,\vec{u}_i}{\partial\,t} + (\vec{u}_i\cdot\nabla)\,\vec{u}_i - \sqrt{\frac{\text{Pr}}{\text{Ra}}}\,\Delta\,\vec{u}_i + \nabla\,p_i - T_i\,\vec{e}_Z\right)^2\right\| \tag{12}$$

$$\mathcal{L}_{\text{EE}} = \frac{1}{N_B}\sum_{i=1}^{N_B^{\text{col}}} \left\|\left(\frac{\partial\,T_i}{\partial\,t} + (\vec{u}_i\cdot\nabla)\,T_i - \sqrt{\frac{1}{\text{Pr Ra}}}\,\Delta\,T_i\right)^2\right\| \tag{13}$$

$$\mathcal{L}_{\text{div}} = \frac{1}{N_B}\sum_{i=1}^{N_B^{\text{col}}} \left\|(\nabla\cdot\vec{u}_i)^2\right\| \tag{14}$$

$$\mathcal{L}_{\text{C}} = \frac{1}{N_B}\sum_{i=1}^{N_B} \left\|(p_i)^2\right\| \tag{15}$$

$$\begin{aligned}\mathcal{L}_{\text{BC}} = {} & \frac{1}{N_{\text{B}}}\sum_{i=1}^{N_{\text{B}}^{\text{col}X}} \left\|\vec{u}(t_i,0,Y_i,Z_i)^2\right\| + \left\|\vec{u}(t_i,1,Y_i,Z_i)^2\right\| + \\ & \frac{1}{N_{\text{B}}}\sum_{i=1}^{N_{\text{B}}^{\text{col}Y}} \left\|\vec{u}(t_i,X_i,0,Z_i)^2\right\| + \left\|\vec{u}(t_i,X_i,1,Z_i)^2\right\| + \\ & \frac{1}{N_{\text{B}}}\sum_{i=1}^{N_{\text{B}}^{\text{col}Z}} \left\|\vec{u}(t_i,X_i,Y_i,0)^2\right\| + \left\|\vec{u}(t_i,X_i,Y_i,1)^2\right\|\end{aligned} \tag{16}$$

The total loss function used to train the PINN is a sum of several mean squared error loss contributions with their corresponding global weight factors λ. The loss contributions are: the data loss $\mathcal{L}_{\mathrm{data}}$, the pressure centering loss $\mathcal{L}_{\mathrm{C}}$ which restricts the pressure to be centered around zero, the boundary loss $\mathcal{L}_{\mathrm{BC}}$ for the velocity, and physical losses: the residual loss $\mathcal{L}_{\mathrm{NS}}$ of the momentum equations (1), the residual loss $\mathcal{L}_{\mathrm{EE}}$ of the energy equation (2), and the loss $\mathcal{L}_{\mathrm{div}}$ due to the incompressibility condition (3). The data given in the data loss term equation (11), e.g. from a DNS or a measurement, are denoted by an asterisk, e.g. $\vec{u}^*$ for a known velocity field. The physical loss terms $\mathcal{L}_{\mathrm{NS}}$, $\mathcal{L}_{\mathrm{EE}}$ and $\mathcal{L}_{\mathrm{div}}$ are not evaluated at the same data points given by the batch N_B as the data loss $\mathcal{L}_{\mathrm{data}}$ and the pressure centering loss $\mathcal{L}_{\mathrm{C}}$ during training. Instead, a new collocated batch of the same size as N_B, called N_B^{col}, is defined per training epoch, containing input data points (t_i, X_i, Y_i, Z_i) randomly uniform distributed within the cubic cell and across all data time steps.

Thus, assuming a long enough training time, the physical loss terms are estimated nearly everywhere in the domain, providing the spatial resolution necessary to capture flow structures on a wide range of scales (Hou et al., 2023). Furthermore, three other collocation batches $N_{\mathrm{B}}^{\mathrm{col}_X}$, $N_{\mathrm{B}}^{\mathrm{col}_Y}$, and $N_{\mathrm{B}}^{\mathrm{col}_Z}$ are defined. Each of them contains N_B randomly uniform distributed input data points, in each of the two pairs of opposite sidewalls, e.g. $X = 0$ and $X = 1$ in the batch $N_{\mathrm{B}}^{\mathrm{col}_X}$ and similarly for the batches with superscript Y and Z. The three collocation batches on the sidewalls of the cube are used to train the loss of the boundary condition $\mathcal{L}_{\mathrm{BC}}$ that suppresses the velocity to zero at each sidewall. Following the idea of constant hierarchical weighting (Mommert et al., 2024), we use fixed weight factors associated with the values shown in table 2. In this approach, weighting factors are introduced for each loss term to control its importance relative to a reference loss term. We choose the data loss with $\lambda_{\mathrm{data}} = 1$ as the reference loss term.

λ_{data}	λ_{NS}	λ_{EE}	λ_{div}	λ_{C}	λ_{BC}
1.0	0.1	0.01	0.001	0.001	0.0001

Table 2. Global weights used in the total loss function of the PINN.

3.3. Evaluation metrics

Two metrics are used to monitor the PINN training process: the mean average error MAE_ζ and the Pearson correlation coefficient PCC_ζ with $\zeta \in \{u, v, w, T, p\}$, and they are defined by:

$$\mathrm{MAE}_\zeta = \frac{1}{N_s} \sum_{i=1}^{N_s} \|\zeta_i - \zeta_i^*\| \,, \tag{17}$$

$$\mathrm{PCC}_\zeta = \frac{N_\mathrm{s}\sum_{i=1}^{N_\mathrm{s}}\zeta_i\zeta_i^* - \sum_{i=1}^{N_\mathrm{s}}\zeta_i\sum_{i=1}^{N_\mathrm{s}}\zeta_i^*}{\sqrt{N_\mathrm{s}\sum_{i=1}^{N_\mathrm{s}}\zeta_i^2 - \left(\sum_{i=1}^{N_\mathrm{s}}\zeta_i\right)^2}\sqrt{N_\mathrm{s}\sum_{i=1}^{N_\mathrm{s}}(\zeta_i^*)^2 - \left(\sum_{i=1}^{N_\mathrm{s}}\zeta_i^*\right)^2}}\,. \tag{18}$$

Here, N_s denotes the number of samples used to calculate the individual metrics. The terms denoted with an asterisk correspond to given data from a DNS or a measurement.

4. PINN validation using synthetic PTV data

The results obtained with the PINN are validated in comparison with results obtained from 150000 synthetic particle trajectories generated in a DNS (section 2.1) of a hard turbulent RBC with $\mathrm{Ra} = 10^9$, $\mathrm{Pr} = 6.9$, which was processed for 125 time steps representing 2.5 free fall time units. The parameter $a = 126$ is chosen to mimic the mean temperature profile and the temperature boundary conditions at the top and bottom plates for the considered case with a Nusselt number $\mathrm{Nu} = 63$. The PINN was trained over 2500 epochs and the training process took about 55 seconds per epoch on a NVIDIA GeForce RTX 4090.

The Pearson correlation coefficients (PCC) of the output fields computed in the course of the training are shown in the left panel of figure 8. The correlation values of the velocity components reach almost 100% with respect to the ground truth. It is noteworthy that the reconstructed temperature and pressure fields also reach correlation values of about 90% with respect to the ground truth at the end of training. The correlation values are not biased by the boundary conditions, since they are estimated at the particle positions, and there are no particles at the boundaries in our dataset. Therefore, correlation values are suitable for comparing the flow structures in the reconstructed fields with those of the ground truth (DNS). Also, the mean average error (MAE) of the reconstructed flow fields compared to the DNS fields are shown in the right panel of figure 8 for the course of the training. The MAE of the velocity components, pressure, and temperature converge to values of about $2 \cdot 10^{-3}$, $1 \cdot 10^{-3}$, and $1 \cdot 10^{-2}$, respectively, after 2500 training epochs. The MAE of the temperature is higher than in all other fields, but the MAE is biased by the higher reconstruction errors in the boundary layers near the heating and cooling plates, where temperature values are large. As we will see later when analyzing figure 14, the temperature reconstruction error is much smaller in the global bulk flow than in the boundary layers. Thus, the temperature MAE does not provide a reasonable value. Both the PCC and MAE values shown in figure 8 are estimated at time step 120 ($\approx 2.4\,t_{ref}$).

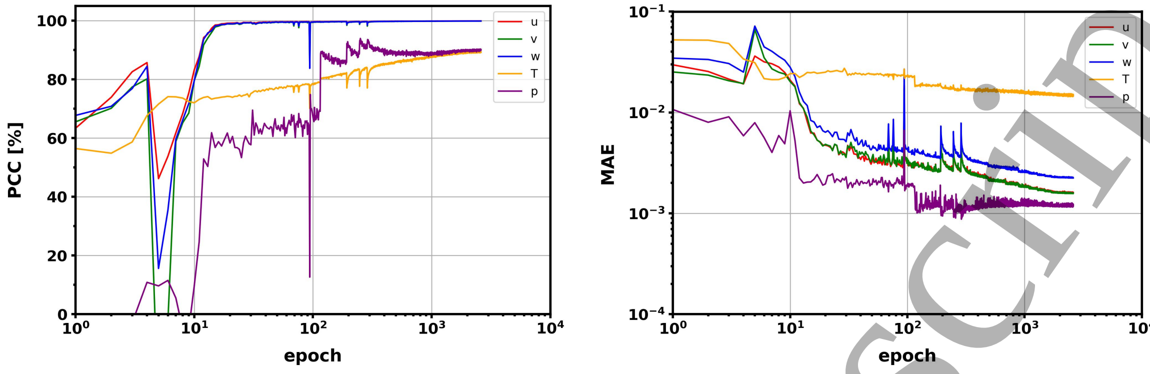

Figure 8. Pearson correlation values (left) and MAE (right) of the velocity components, temperature and pressure estimated from the reconstructed PINN fields compared with the DNS fields over 2500 epochs of training.

Figure 9 shows the dynamic behavior of the PCC and MAE values of each flow field at each time step of the dataset after 2500 epochs of training. The correlation of the velocity fields is almost 100%, except at the beginning and end of the dataset. This is due to a typical data fitting problem: the PINN uses a superposition of sine functions to fit the time dynamics of the velocity fields by optimizing data loss, and an abrupt end to the dataset causes higher fitting errors. The correlation of the temperature and pressure fields increases in time until 2 t_{ref} where the PCC values converges to about 90%. This behavior is known as PINN and presumably needs to be trained over a sufficient time span to learn the dynamics of the flow, and a temporal length of at least 2 t_{ref} is needed, which was shown by Volk et al. (2025).

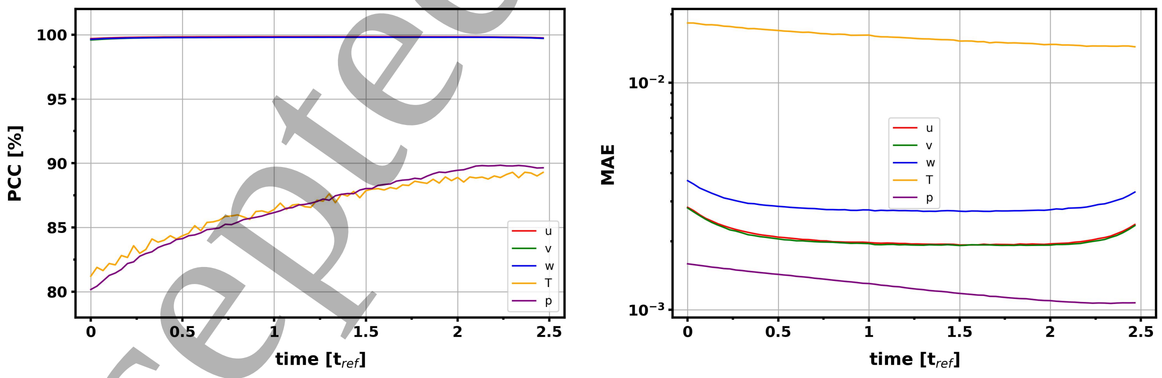

Figure 9. Pearson correlation values (left) and MAE (right) of the velocity components, temperature and pressure estimated from the reconstructed PINN fields compared with the DNS fields at each time step after 2500 epochs of training.

The high correlation values of the reconstructed properties with respect to the ground truth can be visually investigated in figure 10, which provides a visual comparison of the instantaneous vertical velocity, temperature, and pressure fields at time step 120 ($\approx 2.4\, t_{ref}$) of the DNS and their reconstruction using PINN. It is difficult to see differences in velocity and pressure, by comparing the temperature fields color differences can be seen near the cooling plate and in the smaller plume-like structures in the bulk.

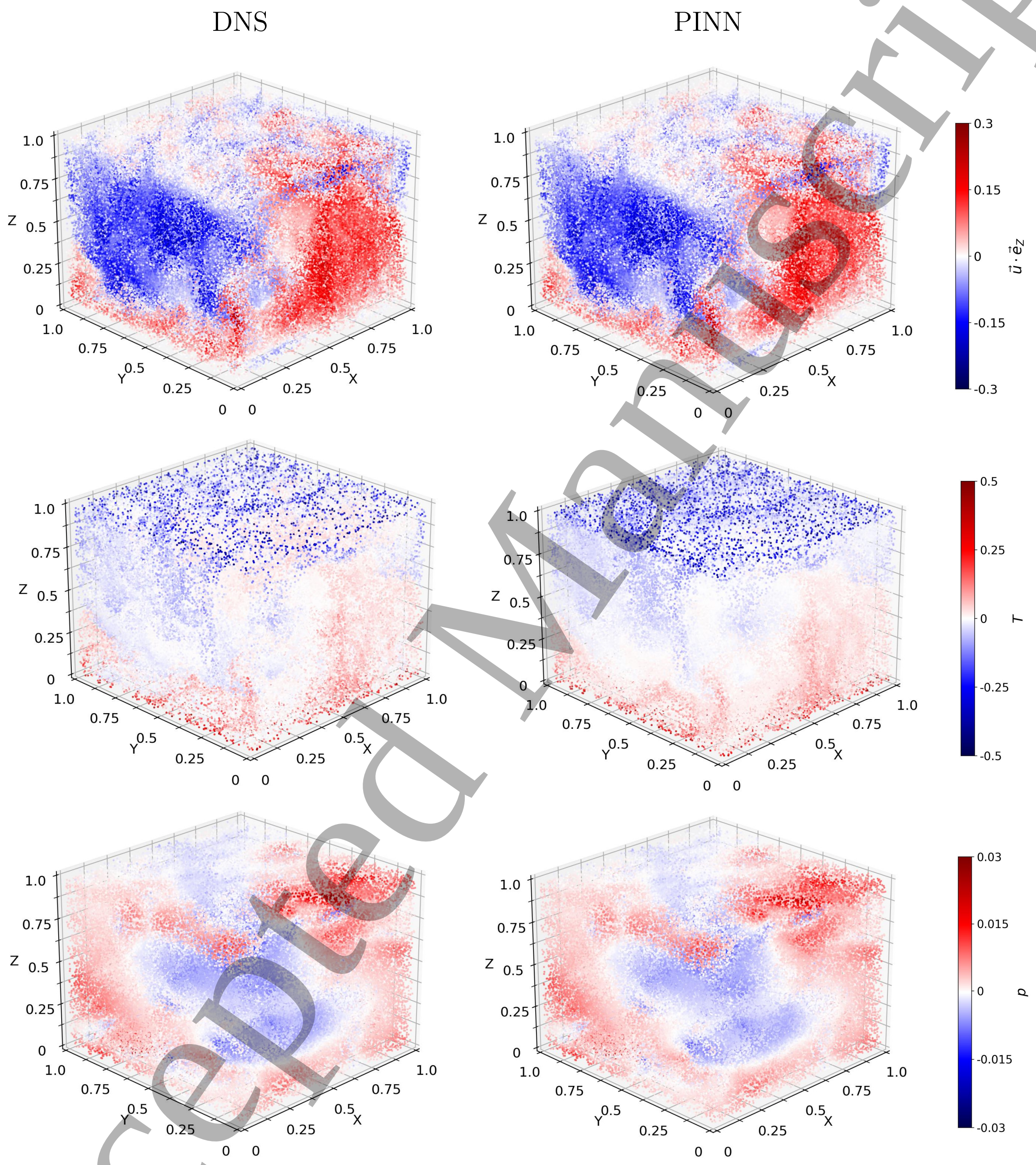

Figure 10. Colored Instantaneous vertical velocity (top), temperature (mid) and pressure (bottom) at the time step 120. Left: DNS vertical velocity, temperature and pressure on the particle positions. Right: reconstructed vertical velocity, temperature and pressure on the particle positions using the PINN.

The differences in the reconstructed temperature field compared to the ground truth temperature are analyzed by comparing their averaged temperature profiles as a function of cell height Z, shown in figure 11. The averaging was performed with respect to the horizontal directions X and Y and over the whole dataset in time. The mean temperature profiles with steep gradients at the walls and the nearly vanishing gradients in the bulk are typical for the considered high Ra number flow with a well mixed bulk region. In principle, the mean temperature profiles agree well, but the profile of the reconstructed temperature deviates from the DNS profile in the boundary layers. To mitigate boundary layer reconstruction errors, Volk et al. (2025) proposed an PINN training approach that restricts collocation point placement in later epochs in regions with higher reconstruction errors, particularly within the boundary layers themselves. This method is not yet implemented in the current code version, but it will help to deal with errors inside the boundary layer in the future.

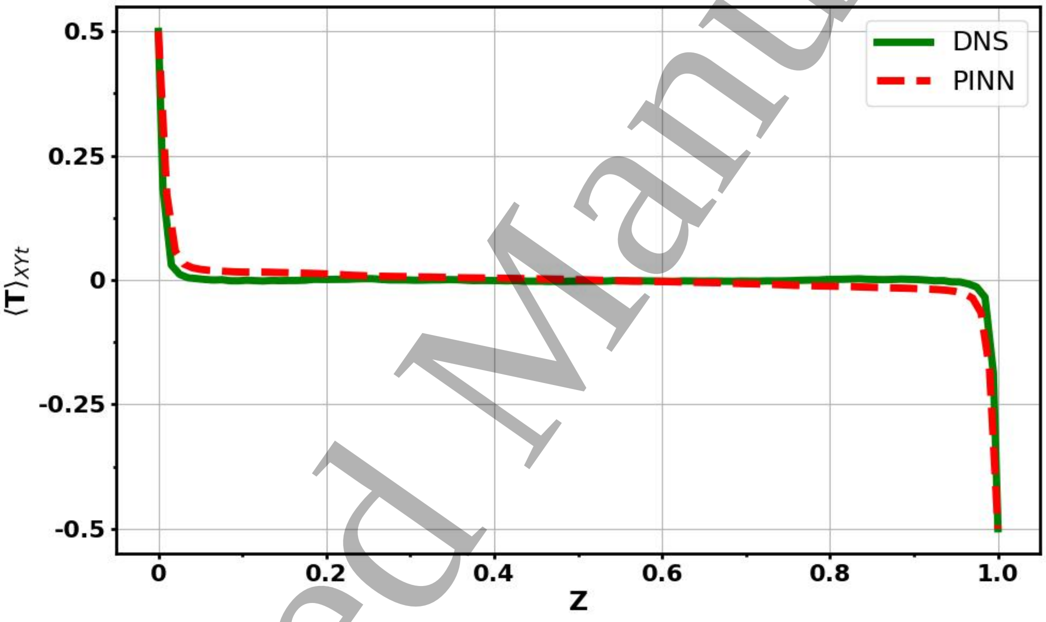

Figure 11. Computed and reconstructed mean temperature profiles $\langle T\rangle_{XYt}$ averaged horizontally and with respect to time as a function of cell height determined from the temperatures of the particles in the DNS and the PINN, respectively.

Figure 12 shows the flow field statistics by comparing the probability density function (PDF) of the reconstructed velocity components, temperature, pressure, and heat flux wT using PINN with those of the DNS dataset. All time steps are used to generate the PDFs. In accordance with the high PCC values at the end of the training, the PDFs of the velocity components obtained from the DNS and the PINN agree well. Also, the PDFs of the temperature shown in figure 12 agree well. However, there are some deviations with more frequent large reconstructed temperature values obtained with the PINN than predicted in the DNS. The reason for this is that the PINN was trained with the exact temperature boundaries, which required the PINN to learn a temperature field that connects the bulk with the boundary values. Therefore, deviations from DNS temperature values occur mainly in the boundary layers, where the absolute temperature and its gradient are high. In contrast, the PDF of the reconstructed pressure shows differences for positive pressure values with the DNS pressure, which has a strongly asymmetric distribution around zero, but at zero and negative pressures the PDFs agree well.

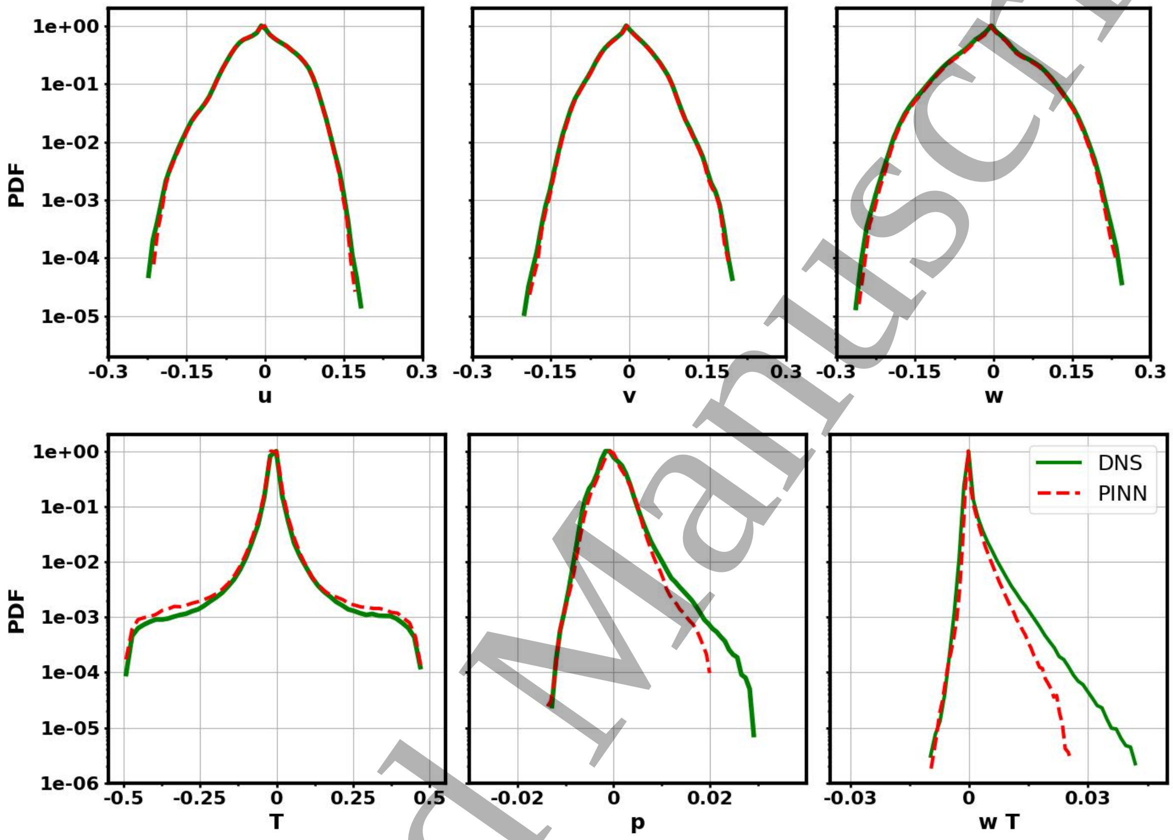

Figure 12. PDFs of the three velocity components, temperature, pressure and heat flux calculated from the synthetic PTV tracks from the DNS in green compared with the PDFs obtained with the PINN results in red.

Compared to the overall picture of the flow given in figure 10, a direct comparison of the reconstructed flow fields with the DNS in the diagonal plane of the cubic cell containing the LSC is given next, since in this plane the most interesting dynamics in the flow can be observed. The corresponding instantaneous DNS velocity components at the particle positions, the reconstructed velocity components, and the difference between these components at time step 120 ($\approx 2\,t_{ref}$) in the diagonal plane of the cubic cell containing the LSC with a thickness of $L/50$ are shown in figure 13 to demonstrate the visual correlation between these fields. Figure 14 shows the corresponding temperature and pressure fields and their differences in the same way. As shown in the bottom row of figure 13, the reconstructed velocity components differ only slightly from the ground truth, consistent with the high PCC values of nearly 100% at the end of training. The error distribution of all velocity components looks similar and only a few patches with a maximum error of about 10% can be found, overall the average relative error with respect to the maximum velocity of 0.3 is about 1% for all velocity components, which is a good result showing that the training of the PINN with respect to the data loss worked perfectly.

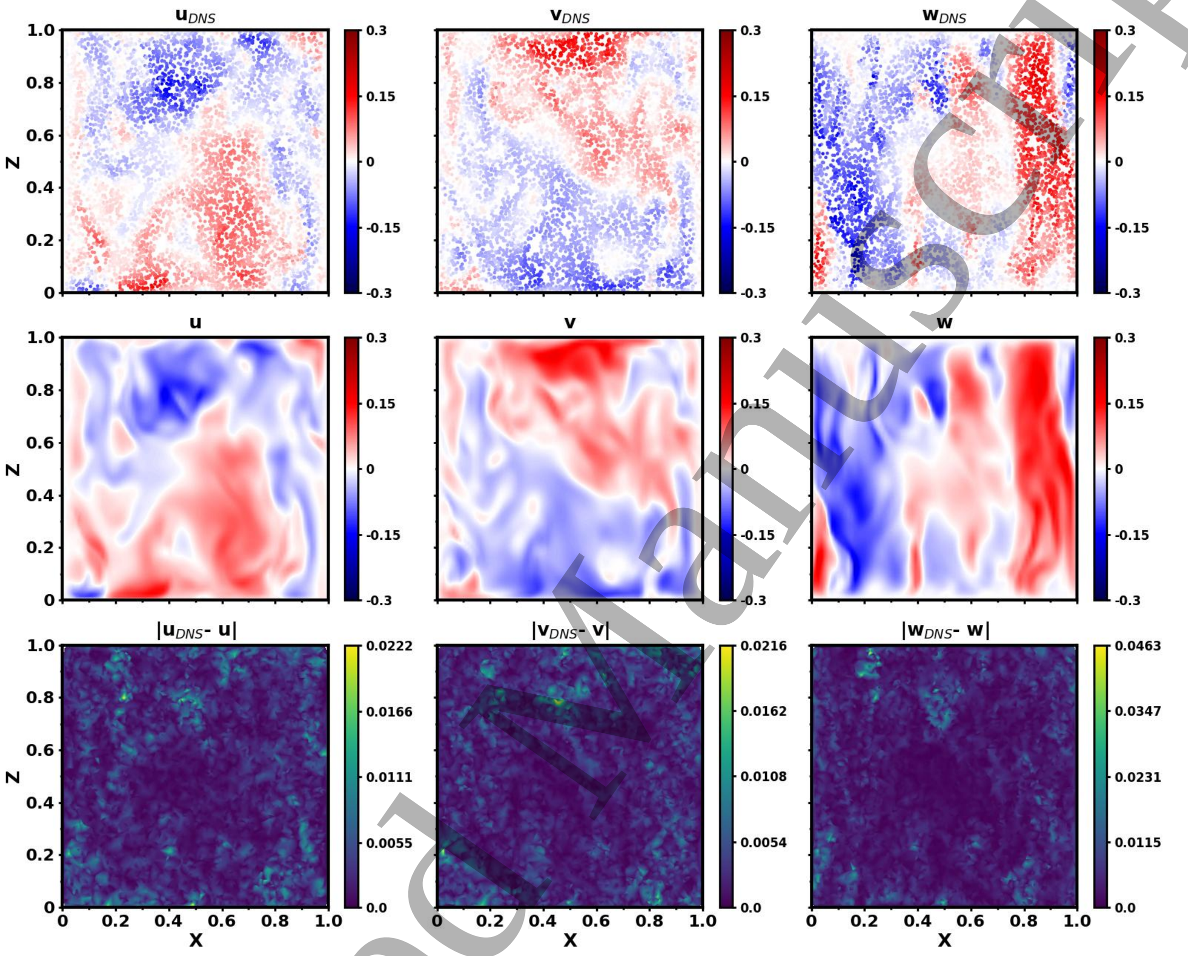

Figure 13. Color contours of the three velocity components in the diagonal plane of the cubic cell containing the LSC with a thickness of $L/50$ predicted in the DNS u_{DNS}, v_{DNS}, w_{DNS} (ground truth) in comparison with the reconstructed velocities u, v, w computed from the synthetic PTV tracks using the PINN. The absolute error between the fields of the same properties is visualized in the bottom row.

The reconstructed temperature and pressure show the highest error near the heating and cooling plate compared to the ground truth, see the bottom row in figure 14. In the bulk, both fields show small errors and the average relative error is about 5% for the temperature and 10% for the pressure. The fact that the largest reconstruction errors are in the boundary layers is consistent with previously discussed results and is due to the lack of data from a well-resolved boundary layer and the lack of a method to correctly reconstruct the boundary layers. Most importantly, the reconstructed temperature and pressure fields behave realistically. The temperature field shows thermal plumes that extend from the heating and cooling plates to the entire cell height, which are also coupled to the motion of the LSC. The pressure field is characterized by pressure minima at the positions of the secondary circulations in the corner and in the center of the LSC.

Pressure maxima are correctly reconstructed at the position where the LSC interacts with the boundaries.

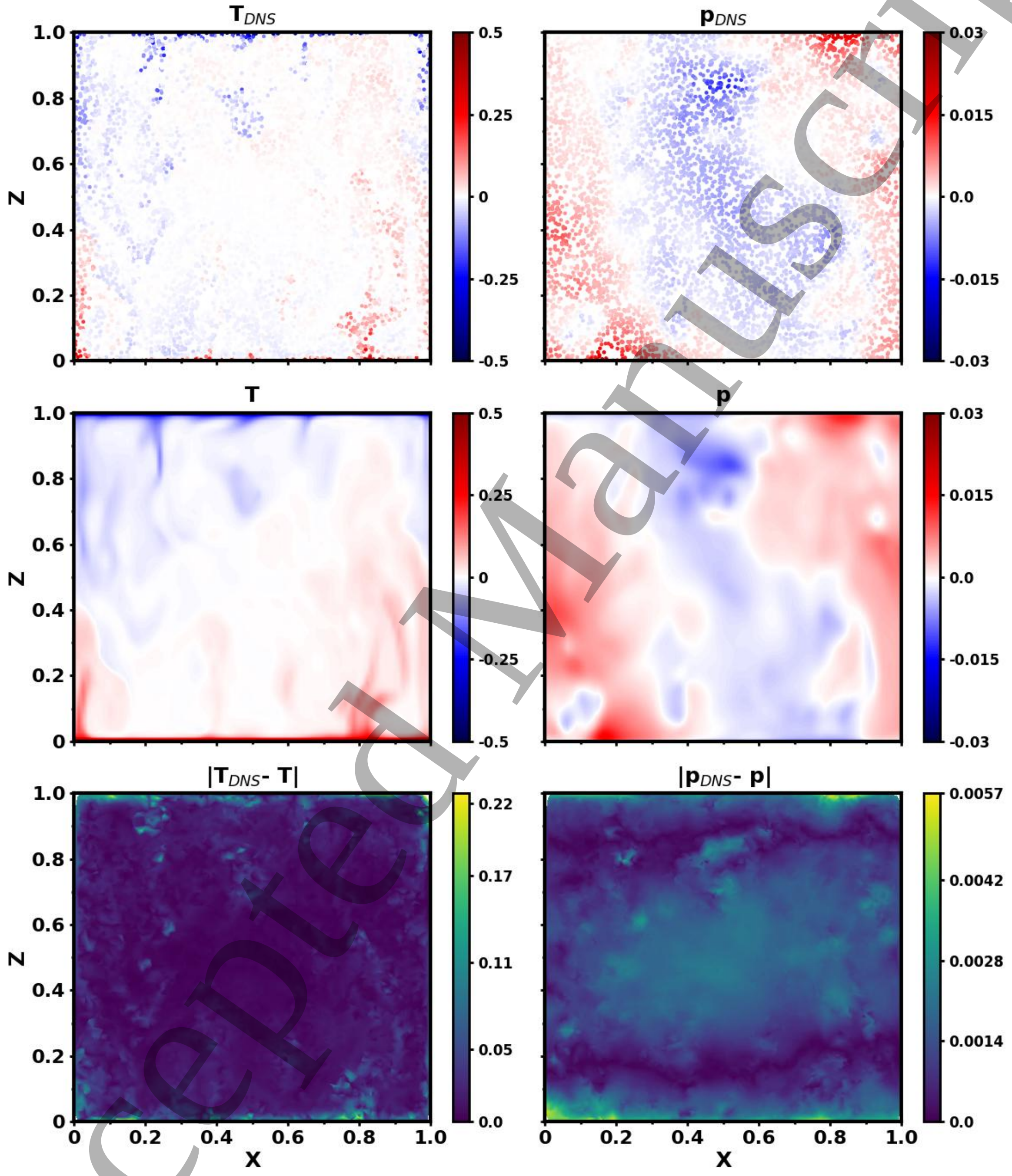

Figure 14. Color contours of the pressure and temperature in the diagonal plane of the cubic cell containing the LSC with a thickness of $L/50$ predicted in the DNS T_{DNS}, p_{DNS} (ground truth) in comparison with the reconstructed properties T, p computed from the synthetic PTV tracks using the PINN. The absolute error between the fields of the same properties is visualized in the bottom row.

The physical response in RBC is measured by the Nusselt number, which describes the dominance of convective heat transport over conductive heat transport, and we know that the time and space averaged Nusselt number in the DNS is approximately $\mathrm{Nu} = 63.4$ for system parameters $\mathrm{Ra} = 10^9$ and $\mathrm{Pr} = 6.9$. Thus, we can verify whether the PINN reconstructs a flow with the correct physical heat flux over the cell height by calculating the Nusselt number with equation (6), resulting in $\mathrm{Nu}_{\mathrm{PINN}} = 61.8$. The resulting Nu deviates only a little from the Nu value obtained in the DNS. Thus, we can expect that the PINN provides a realistic flow. Note that the averaging interval of $2.5\,t_{ref}$ is not sufficient for complete statistical convergence of Nu in the current dataset.

5. Temperature and pressure reconstruction using experimental PTV data

In the following, the temperature and pressure reconstruction with the proposed PINN is tested using the velocity fields of an experimental PTV dataset ($\mathrm{Ra} \approx 10^9$, $\mathrm{Pr} \approx 6.9$), see section 2.2, consisting of nearly 300000 particle trajectories over 150 time steps, of which about 50000 are active per time step. The dataset covers a similar time span as the DNS dataset of 2.5 free fall time units. The parameter $a = 126$ is chosen to mimic the mean temperature profile and temperature boundary conditions at the top and bottom plates for the considered case with a Nusselt number $\mathrm{Nu} \approx 63$, known from the DNS for similar system parameters. The PINN was trained over 2500 epochs and the training process took about 38 seconds per epoch on a NVIDIA GeForce RTX 4090. The particle positions and velocities measured in the PTV experiments are associated with calibration and image processing errors. It is well known that the velocity component u in the direction of the cameras is associated with the largest error. Thus, reconstructing physical flow fields with a PINN provides a method for processing experimental data while maintaining physical consistency with the governing equations (1)-(3) and reducing measurement uncertainties, as shown in figure 15 where the measured velocities (top row) are compared with the reconstructed velocity (middle row) at the particle positions in the diagonal plane of the cubic cell containing the LSC with a thickness of $L/20$ at time step 145. The bottom row shows the absolute error of the reconstructed velocities with respect to the measured velocities. It is clear that the experiment does not resolve boundary layers, since the particle density reduces to zero near the sidewalls in figure 15. However, the PINN can reconstruct unmeasured flow properties. In our case this means to construct the temperature and pressure fields, which are shown in figure 16 in the diagonal plane of the cubic cell containing the LSC at time step 145. The reconstructed temperature and pressure fields show realistic results compared to figure 14. The temperature field features thermal plumes of integral length that detach from the heating and cooling plates and are coupled to the motion of the LSC. In addition, pressure minima are located in the center of the LSC, and in corner circulations, while pressure maxima are constructed in regions where the LSC interacts with the boundaries.

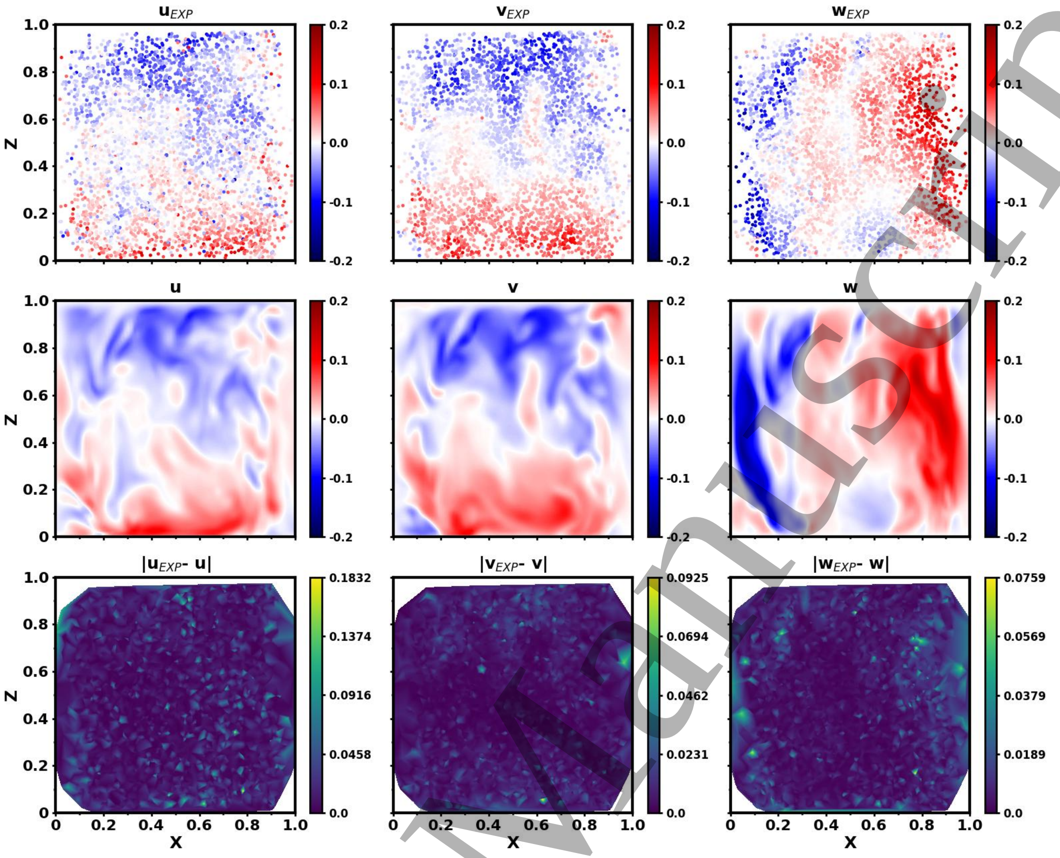

Figure 15. Color contours of the three velocity components in the diagonal plane of the cubic cell containing the LSC with a thickness of $L/20$ measured with PTV experimentally u_{EXP}, v_{EXP}, w_{EXP} in comparison with the reconstructed velocities u, v, w computed using the PINN. The absolute error between the fields of the same properties is visualized in the bottom row.

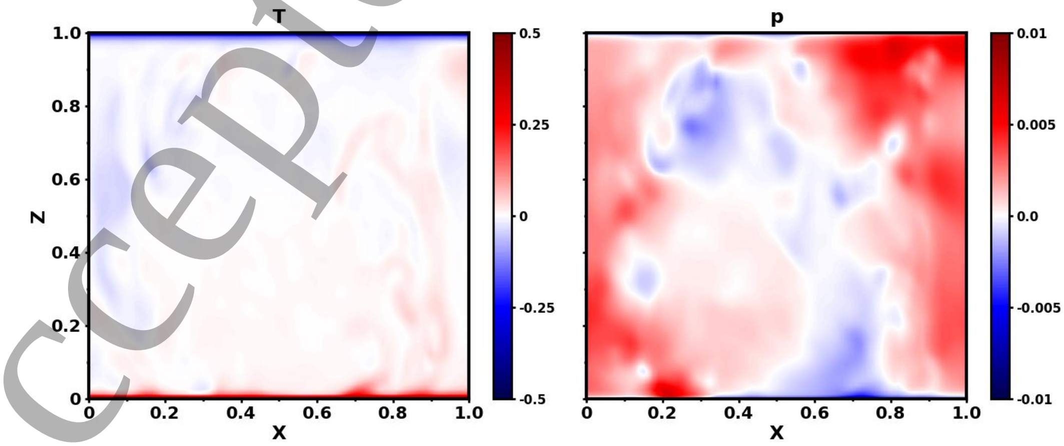

Figure 16. Temperature field T and pressure field p in the diagonal plane of the cubic cell containing the LSC constructed with the PINN based on experimental PTV tracks.

Figure 17 shows the probability density function (PDF) of the constructed velocity components, temperature, pressure, and heat flux wT using the PINN. In the top row of figure 17 the PDFs of the velocity components are compared with those obtained from the measured velocities. The PINN reconstructs a similar distribution for the velocity components v and w as provided by the experiment.

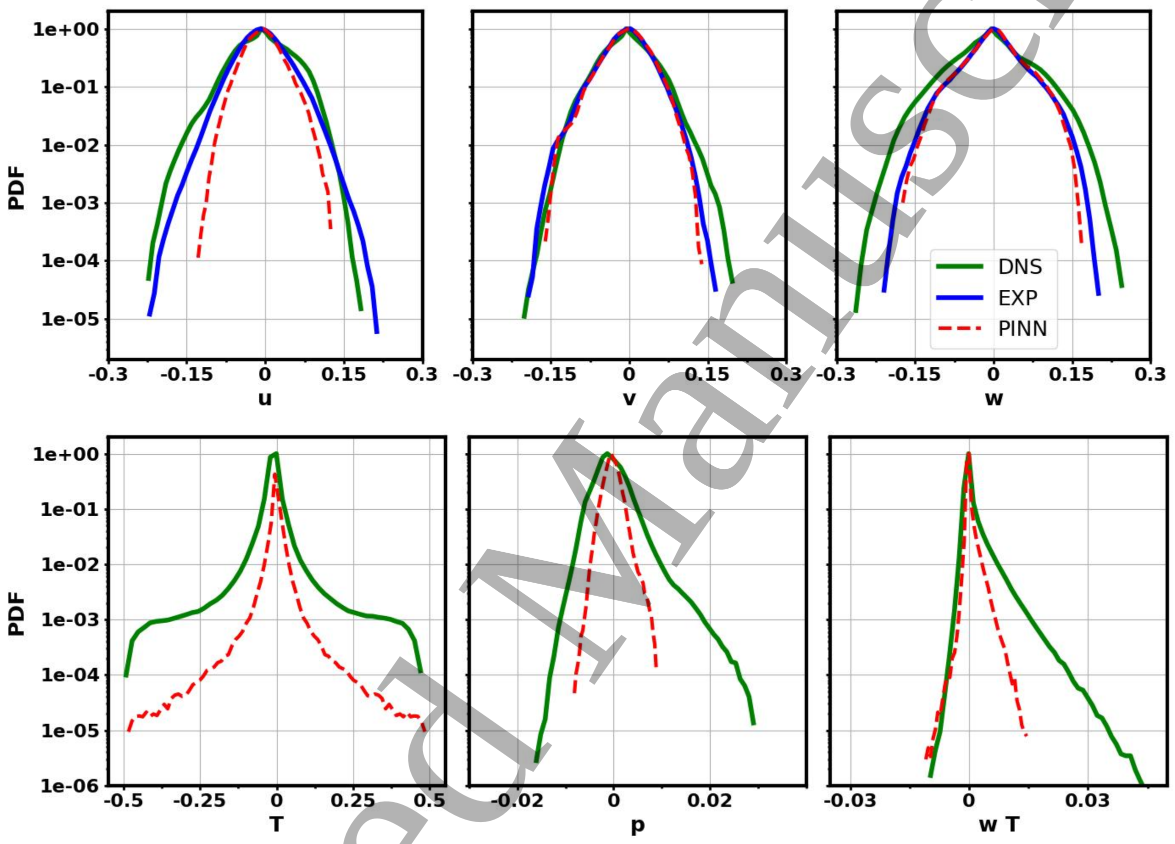

Figure 17. PDFs of the three velocity components, temperature, pressure and heat flux calculated from the experimental PTV tracks in blue compared with the PDFs obtained with the PINN results in red, and the PDFs obtained from the DNS taken from figure 12 are shown in green.

The PDF of u in the experimental data exhibits bias due to measurement uncertainties, as this component corresponds to the depth direction X of the camera system. While the PINN successfully denoises the experimental data while preserving physical consistency, the reconstructed PDF of u shows a reduction in extreme values compared to the DNS reference data. Given the inherent measurement uncertainties in the u-component, improved reconstruction accuracy might be achieved by independently adjusting the data loss weight for this velocity component during training, separate from the weighting parameters applied to the other velocity components. However, preliminary testing of this approach yielded no significant improvements, suggesting that a more systematic investigation of optimal weight factor selection would be beneficial. The bottom row of figure 17 presents the PDFs of the purely reconstructed quantities: temperature, pressure, and convective heat flux. The temperature PDF exhibits the expected characteristic bimodal distribution, though with fewer high absolute temperature values compared to the DNS reference. This discrepancy is attributed to the absence of well-resolved boundary layers in the experimental data, which the PINN consequently cannot reconstruct accurately. The pressure PDF demonstrates a similar trend of reduced extreme values relative to the DNS data. The convective heat flux PDF maintains the same overall shape as that obtained from PINN reconstruction of DNS data (Figure 12), but similarly shows fewer high absolute values. Notably, both the reconstructed heat flux PDFs lack the asymmetry toward positive values that characterizes the DNS reference data, indicating potential limitations in capturing the full range of heat transport dynamics.

The physical response of the reconstructed flow is evaluated using the reconstructed vertical velocity and temperature to calculate the averaged Nusselt number using equation (6), resulting in $\mathrm{Nu}_{\mathrm{PINN}} = 34.6$. Note that the averaging interval is not sufficient for complete statistical convergence of Nu in the current dataset. The deviation from the reference value at $\mathrm{Nu} \approx 63$ is explained by examining the color scales of the particle tracks in figures 4 and 1, where it can be seen that the vertical velocity scale of the DNS tracks is about a factor of 1.6 larger than that of the measured tracks. In an ideal setup, such as the DNS, RBC involves adiabatic side walls, which are absent in our experiment. Instead, we used glass sidewalls with 8 mm thickness to provide optical access for PTV measurements. This configuration results in an estimated total relative heat loss through the side walls of approximately 20%. This heat loss diminishes a portion of the buoyancy forcing that drives the LSC, which consequently reduces the maximum normalized vertical velocity compared to DNS. This reduction is clearly observable: the maximum normalized vertical velocity is about 0.29 in the DNS versus 0.18 in the experiment. Applying the corrective factor of 1.6 to the estimated averaged Nusselt number yields $\mathrm{Nu} = 55.3$. The remaining discrepancy between this value and the expected value of about 63 is based on measurement uncertainties in the experimental procedure and reconstruction errors of the proposed method.

6. Conclusion

This study successfully demonstrates the application of a physics-informed neural network (PINN) to reconstruct temperature and pressure fields from Lagrangian velocity data in turbulent Rayleigh-Bénard convection (RBC) at $\mathrm{Ra} = 10^9$ and $\mathrm{Pr} = 7$, utilizing both synthetic direct numerical simulation (DNS) and experimental particle tracking velocimetry (PTV) datasets. The PINN, employing a multilayer perceptron architecture with a periodic sine activation function, incorporates a modification by adding a mean temperature profile to the temperature output, as defined in equation (7). This profile, parameterized by $a = 2\,\mathrm{Nu}$, ensures exact satisfaction of the temperature boundary conditions and facilitates accurate reconstruction of temperature fluctuations, particularly in the well-mixed bulk region, thus addressing the numerical challenges

posed by high temperature gradients in the hard turbulence regime.
In the DNS case, the PINN is able to reconstruct temperature and pressure fields with a correlation of 90% with respect to the ground truth. For this high correlation factor the associated flow fields consist of thermal plumes, large-scale circulation, and pressure variations at the correct locations as the comparison with DNS data shows. However, the reconstruction effectiveness is limited in the thermal and viscous boundary layers due to insufficient particle data near the walls and the PINN's lack of specialized training for these regions. This limitation results in deviations in the temperature profiles near the boundaries, as observed in figure 11. When applied to experimental PTV data, the PINN not only constructs physically consistent temperature and pressure fields but also reduces measurement uncertainties in the velocity fields, demonstrating its robustness in handling noisy experimental data. The reconstructed Nusselt number profile in the bulk flow deviates from the expected value due to heat losses through non-adiabatic glass sidewalls, which diminish buoyancy-driven flow compared to the ideal DNS setup. In future experiments, the thickness of the side walls should be increased to compensate this effect. However, PINN reproduces realistic integral flow structures, such as thermal plumes and pressure minima in circulatory regions, highlighting its ability to assimilate unmeasured flow properties in complex convective systems. The compatibility of the PINN with the open-source proPTV framework represents a significant advancement, enabling comprehensive flow analysis without direct measurements of all flow quantities. The PINN code, available at `https://github.com/DLR-AS-BOA/RBC-PINN`, supports further development and application across diverse flow scenarios. While the proposed methodology excels in reconstructing bulk flow dynamics, future improvements should focus on enhancing boundary layer reconstruction, potentially by adopting and refining the boundary-focused training strategies proposed by Volk et al. (2025) or incorporating additional physical constraints to account for experimental non-ideal, such as non-adiabatic boundaries. These advancements will further strengthen the applicability of PINNs in studying turbulent thermal convection and other complex flow systems.

References

Martín Abadi, Ashish Agarwal, Paul Barham, Eugene Brevdo, Zhifeng Chen, Craig Citro, Greg S. Corrado, Andy Davis, Jeffrey Dean, Matthieu Devin, Sanjay Ghemawat, Ian Goodfellow, Andrew Harp, Geoffrey Irving, Michael Isard, Yangqing Jia, Rafal Jozefowicz, Lukasz Kaiser, Manjunath Kudlur, Josh Levenberg, Dan Mane, Rajat Monga, Sherry Moore, Derek Murray, Chris Olah, Mike Schuster, Jonathon Shlens, Benoit Steiner, Ilya Sutskever, Kunal Talwar, Paul Tucker, Vincent Vanhoucke, Vijay Vasudevan, Fernanda Viegas, Oriol Vinyals, Pete Warden, Martin Wattenberg, Martin Wicke, Yuan Yu, and Xiaoqiang Zheng. Tensorflow: Large-scale machine learning on heterogeneous distributed systems. *arXiv preprint*, 2016. URL `https://doi.org/10.48550/ARXIV.1603.04467`.

Robin Barta and Claus Wagner. Large-scale reorientation in cubic rayleigh–bénard convection measured with particle tracking velocimetry. *Journal of Turbulence*, pages 1–14, 2025. URL `https://doi.org/10.1080/14685248.2024.2436843`.

Robin Barta, Christian Bauer, Sebastian Herzog, Daniel Schiepel, and Claus Wagner. proptv: A probability-based particle tracking velocimetry framework. *Journal of computational physics*, 2023. URL `https://doi.org/10.1016/j.jcp.2024.113212`.

Shengze Cai, Zhiping Mao, Zhicheng Wang, Minglang Yin, and George Em Karniadakis. Physics-informed neural networks (pinns) for fluid mechanics: A review. *Acta Mechanica Sinica*, 37(12):1727–1738, 2021a. URL `https://doi.org/10.1007/s10409-021-01148-1`.

Shengze Cai, Zhicheng Wang, Frederik Fuest, Young Jin Jeon, Callum Gray, and George Em Karniadakis. Flow over an espresso cup: inferring 3-d velocity and pressure fields from tomographic background oriented Schlieren via physics-informed neural networks. *Journal of Fluid Mechanics*, 915, 2021b. URL `https://doi.org/10.1017/jfm.2021.135`.

Bernard Castaing, Gemunu Gunaratne, Francois Heslot, and Gianluigi Zanetti. Scaling of hard thermal turbulence in rayleigh-bénard convection. *Journal of Fluid Mechanics*, 204:1–30, 1989. URL `https://doi.org/10.1017/S0022112089001643`.

François Chollet et al. Keras, 2015. URL `https://keras.io`.

Patricio Clark Di Leoni, Lokahith Agasthya, Michele Buzzicotti, and Luca Biferale. Reconstructing rayleigh–bénard flows out of temperature-only measurements using physics-informed neural networks. *The European Physical Journal E*, 46(3):16, 2023. URL `https://doi.org/10.1140/epje/s10189-023-00276-9`.

Donald D Gray and Aldo Giorgini. The validity of the boussinesq approximation for liquids and gases. *International Journal of Heat and Mass Transfer*, 19(5):545–551, 1976. URL `https://doi.org/10.1016/0017-9310(76)90168-X`.

Siegfried Grossmann and Detlef Lohse. Scaling in thermal convection: A unifying theory. *Journal of Fluid Mechanics*, 407:27–56, 2000. URL `https://doi.org/10.1017/S0022112099007545`.

Siegfried Grossmann and Detlef Lohse. Thermal convection for large prandtl numbers. *Physical Review Letters*, 86:3316–3319, 2001. URL `https://doi.org/10.1103/PhysRevLett.86.3316`.

Siegfried Grossmann and Detlef Lohse. Prandtl and Rayleigh number dependence of the Reynolds number in turbulent thermal convection. *Physical Review E*, 66, 2002. URL `https://doi.org/10.1103/PhysRevE.66.016305`.

Siegfried Grossmann and Detlef Lohse. Fluctuations in turbulent Rayleigh-Bénard convection: The role of plumes. *Physics of Fluids*, 16:4462–4472, 2004. URL `https://doi.org/10.1063/1.1807751`.

Günther Grötzbach. Spatial resolution requirements for direct numerical simulation of the Rayleigh-Bénard convection. *Journal of Computational Physics*, 49:241–264, 1983. URL `https://doi.org/10.1016/0021-9991(83)90125-0`.

Sebastian Herzog, Daniel Schiepel, Isabella Guido, Robin Barta, and Claus Wagner. A probabilistic particle tracking framework for guided and brownian motion systems with high particle densities. *SN Computer Science*, 2:1–20, 2021. URL https://doi.org/10.1007/s42979-021-00879-z.

Jie Hou, Ying Li, and Shihui Ying. Enhancing pinns for solving pdes via adaptive collocation point movement and adaptive loss weighting. *Nonlinear Dynamics*, 111 (16):15233–15261, 2023. URL https://doi.org/10.1007/s11071-023-08654-w.

T Käufer and C Cierpka. Volumetric lagrangian temperature and velocity measurements with thermochromic liquid crystals. *Measurement Science and Technology*, 35(3): 035301, 2023. URL https://doi.org/10.1088/1361-6501/ad16d1.

Diederik P. Kingma and Jimmy Ba. Adam: A method for stochastic optimization. *arXiv preprint*, 2014. URL https://doi.org/10.48550/ARXIV.1412.6980.

Didier Lucor, Atul Agrawal, and Anne Sergent. Simple computational strategies for more effective physics-informed neural networks modeling of turbulent natural convection. *Journal of Computational Physics*, 456:111022, 2022. URL https://doi.org/10.1016/j.jcp.2022.111022.

HG Maas, A Gruen, and D Papantoniou. Particle tracking velocimetry in three-dimensional flows. *Experiments in Fluids*, 15:133–146, 1993. URL https://doi.org/10.1007/BF00190953.

NA Malik, Th Dracos, and DA Papantoniou. Particle tracking velocimetry in three-dimensional flows. *Experiments in Fluids*, 15:279–294, 1993. URL https://doi.org/10.1007/BF00223406.

Michael Mommert, Robin Barta, Christian Bauer, Marie-Christine Volk, and Claus Wagner. Periodically activated physics-informed neural networks for assimilation tasks for three-dimensional rayleigh–bénard convection. *Computers and Fluids*, 283: 106419, 2024. URL https://doi.org/10.1016/j.compfluid.2024.106419.

Maziar Raissi, Paris Perdikaris, and George E Karniadakis. Physics-informed neural networks: A deep learning framework for solving forward and inverse problems involving nonlinear partial differential equations. *Journal of Computational physics*, 378:686–707, 2019. URL https://doi.org/10.1016/j.jcp.2018.10.045.

Lord Rayleigh. On convection currents in a horizontal layer of fluid, when the higher temperature is on the under side. *The London, Edinburgh, and Dublin Philosophical Magazine and Journal of Science*, 32(192):529–546, 1916. URL https://doi.org/10.1080/14786441608635602.

Shyam Sankaran, Hanwen Wang, Leonardo Ferreira Guilhoto, and Paris Perdikaris. On the impact of larger batch size in the training of physics informed neural networks. In *The Symbiosis of Deep Learning and Differential Equations II*, 2022. URL https://openreview.net/forum?id=THCvohg1RV.

Janet D Scheel, Mohammad S Emran, and Jörg Schumacher. Resolving the fine-scale structure in turbulent rayleigh–bénard convection. *New Journal of Physics*, 15(11): 113063, 2013. URL https://doi.org/10.1088/1367-2630/15/11/113063.

Daniel Schmeling, Andrei Shishkin, Daniel Schiepel, and Claus Wagner. Numerical and experimental study of aerosol dispersion in the Do728 aircraft cabin. *CEAS Aeronautical Journal*, 14:509526, 2023. https://doi.org/10.1007/s13272-023-00644-3.

Andreas Schröder and Daniel Schanz. 3d Lagrangian particle tracking in fluid mechanics. *Annual Review of Fluid Mechanics*, 55, 2023. URL https://doi.org/10.1146/annurev-fluid-031822-041721.

Olga Shishkina, Richard J A M Stevens, Siegfried Grossmann, and Detlef Lohse. Boundary layer structure in turbulent thermal convection and its consequences for the required numerical resolution. *New Journal of Physics*, 12, 2010. URL https://doi.org/10.1088/1367-2630/12/7/075022.

Vincent Sitzmann, Julien Martel, Alexander Bergman, David Lindell, and Gordon Wetzstein. Implicit neural representations with periodic activation functions. *Advances in neural information processing systems*, 33:7462–7473, 2020. URL https://doi.org/10.48550/ARXIV.2006.09661.

Steven M Soloff, Ronald J Adrian, and Zi-Chao Liu. Distortion compensation for generalized stereoscopic particle image velocimetry. *Measurement Science and Technology*, 8, 1997. URL https://doi.org/10.1088/0957-0233/8/12/008.

Juan Diego Toscano, Theo Käufer, Zhibo Wang, Martin Maxey, Christian Cierpka, and George Em Karniadakis. Inferring turbulent velocity and temperature fields and their statistics from lagrangian velocity measurements using physics-informed kolmogorov-arnold networks. *arXiv preprint*, 2024. URL https://doi.org/10.48550/ARXIV.2407.15727.

Juan Diego Toscano, Theo Käufer, Zhibo Wang, Martin Maxey, Christian Cierpka, and George Em Karniadakis. Aivt: Inference of turbulent thermal convection from measured 3d velocity data by physics-informed kolmogorov-arnold networks. *Science advances*, 11(19):eads5236, 2025. URL https://doi.org//10.1126/sciadv.ads5236.

Marie-Christine Volk, Anne Sergent, Didier Lucor, Michael Mommert, Christian Bauer, and Claus Wagner. A pinn methodology for temperature field reconstruction in the piv measurement plane: Case of Rayleigh-B'enard convection. *arXiv preprint arXiv:2503.23801*, 2025.

Claus Wagner, Rainer Friedrich, and Ranga Narayanan. Comments on the numerical investigation of Rayleigh and Marangoni convection in a vertical circular cylinder. *Physics of Fluids*, 6:1425–1433, 1994. URL https://doi.org/10.1063/1.868257.

S Weiss, Ms Emran, and O Shishkina. What rayleigh numbers are achievable under oberbeck–boussinesq conditions? *Journal of Fluid Mechanics*, 986(R2), 2024. URL https://doi.org/10.1017/jfm.2024.389.

B Wieneke. Volume self-calibration for 3d particle image velocimetry. *Experiments in Fluids*, 45:549–556, 2008. URL https://doi.org/10.1007/s00348-008-0521-5.